Effect of climate on interannual variability of terrestrial CO_2 fluxes

Kevin Schaefer,[1] A. Scott Denning,[1] Neil Suits,[1] Jörg Kaduk,[2] Ian Baker,[1] Sietse Los,[3] and Lara Prihodko[1]

Received 6 May 2002; revised 22 August 2002; accepted 23 August 2002; published 27 November 2002.

[1] We evaluated how climate influences interannual variability in the terrestrial Net Ecosystem Exchange (NEE) of CO_2 using the Simple Biosphere Model, Version 2 (SiB2) for 1983 to 1993 on a global, 1° by 1° latitude/longitude grid with a 10-min time step. We quantified climate influences on NEE, explained regional differences, and related NEE variability to the Arctic Oscillation (AO) and the El Niño-Southern Oscillation (ENSO). The simulated NEE reproduces the salient features and magnitude of the measured global CO_2 growth rate. The Northern Hemisphere shows a pattern of alternating positive and negative NEE anomalies that cancel such that the tropics dominate the global simulated NEE interannual variability. Climate influences have strong regional differences with precipitation dominating in the tropics and temperature in the extratropics. In tropical regions with drier soils, precipitation control of photosynthesis (i.e., drought stress) dominates; in nearly saturated soils, precipitation control of respiration dominates. Because of cancellation and competing effects, no single climate variable controls global or regional NEE interannual variability. Globally, precipitation accounts for 44% of NEE variability; followed by Leaf Area Index (23%), soil carbon (12%), and temperature (16%). The influence of ENSO on NEE variability is consistent with that expected for shifting precipitation patterns in the tropics. Except in northern Europe, temperature advection by the AO does not significantly influence NEE variability. Neither the AO nor ENSO fully explain the temperature influence on respiration or the simulated NEE anomaly pattern in the Northern Hemisphere. *INDEX TERMS:* 0315 Atmospheric Composition and Structure: Biosphere/atmosphere interactions; 1610 Global Change: Atmosphere (0315, 0325); 1615 Global Change: Biogeochemical processes (4805); 3322 Meteorology and Atmospheric Dynamics: Land/atmosphere interactions; *KEYWORDS:* carbon dioxide fluxes, terrestrial CO_2 fluxes, net ecosystem production, net ecosystem exchange, climate variability, interannual variability

Citation: Schaefer, K., A. S. Denning, N. Suits, J. Kaduk, I. Baker, S. Los, and L. Prihodko, Effect of climate on interannual variability of terrestrial CO_2 fluxes, *Global Biogeochem. Cycles*, *16*(4), 1102, doi:10.1029/2002GB001928, 2002.

1. Introduction

[2] The measured atmospheric CO_2 growth rate is only about half that expected based on fossil fuel emissions. Modeling, isotope, and inversion studies place much of this "missing sink" in the Northern Hemisphere terrestrial biosphere, but its spatial distribution is not well known. The global, atmospheric CO_2 growth rate shows a great deal of interannual variability [*Conway et al.*, 1994; *Lloyd*, 1999; *Rayner and Law*, 1999; *Tans and Wallace*, 1999; *Bousquet et al.*, 2000; *Fung*, 2000]. The ocean fluxes show relatively low variability [*Rayner and Law*, 1999; *Le Quéré et al.*, 2000], so the growth rate variability is attributed primarily to changes in the terrestrial sink [*Sarmiento*, 1993; *Conway et al.*, 1994; *Trolier et al.*, 1996; *Kaduk and Heimann*, 1997; *LLoyd*, 1999; *Houghton et al.*, 1998; *Tans and Wallace*, 1999; *Houghton*, 2000; *Prince et al.*, 2000]. The large variability in land fluxes makes it difficult to determine long-term trends in the terrestrial sink [*Fung*, 2000]. Climate, land use change, natural disturbance, CO_2 fertilization, and nitrogen deposition all affect terrestrial CO_2 fluxes [*Conway et al.*, 1994; *Bousquet et al.*, 2000; *Fung*, 2000; *Houghton*, 2000]. Climate may be the most important contributor to interannual variability [*Houghton*, 2000], but how it controls net terrestrial CO_2 fluxes is unclear.

[3] Lacking direct measurements of net global CO_2 fluxes, we estimate net terrestrial fluxes from satellite data, inversions, and models. Satellite data, for example, the Normalized Difference Vegetation Index (NDVI), is used to estimate the Leaf Area Index, which, in combination with a model, is used to estimate global net primary production [e.g., *Goetz et al.*, 2000; *Ichii et al.*, 2001]. Since NDVI does not contain direct information about respiration, we

[1]Department of Atmospheric Science, Colorado State University, Fort Collins, Colorado, USA.
[2]Department of Geography, University of Leicester, Leicester, United Kingdom.
[3]Department of Geography, University of Wales, Swansea, United Kingdom.

0886-6236/02/2002GB001928$12.00

cannot use it to estimate net terrestrial fluxes. Inversions can estimate net fluxes for large, continental scale regions, but cannot isolate the exact causes of variability [e.g., *Bousquet et al.*, 2000]. Terrestrial carbon models range from highly mechanistic biogeochemical process models to statistical regression and bookkeeping models. Biogeochemistry models track the amount of carbon in various biological pools [e.g., *Ichii et al.*, 2001], but vary widely in the number of pools and how explicitly they represent photosynthesis and respiration processes. Many of these suggest temperature and precipitation have the most influence on interannual variability, but disagree on the exact mechanism [e.g., *Kaduk and Heimann*, 1997; *LLoyd*, 1999; *Dickinson*, 2000; *Houghton*, 2000]. The influence of climate variability differs considerably between ecosystems and regions with respiration dominating in some areas [*Houghton*, 2000] and photosynthesis in others [*Kaduk and Heimann*, 1997]. How available light and humidity influence CO_2 flux variability is not known.

[4] To quantify the effects of climate interannual variability on terrestrial CO_2 fluxes, we calculated photosynthesis and respiration using a land surface model of leaf- and canopy-level photosynthesis and ecosystem respiration. We use the process information in the model to quantify how each climate variable influences the interannual variability of terrestrial CO_2 fluxes and explain regional and ecosystem differences. Past research emphasized validation of models against measurements from the global CO_2 flask network, comparisons between models [e.g., *McGuire et al.*, 2001], and the partition between land and ocean CO_2 fluxes [e.g., *Houghton*, 2000]. Recent research emphasizes what factors (climate, land use, etc.) most influence the interannual variability of NDVI [*Los et al.*, 2001] and terrestrial CO_2 fluxes [*Kaduk and Heimann*, 1997; *Potter and Klooster*, 1999]. We quantify how interannual climate variability affects terrestrial CO_2 fluxes and relate the results to known climatic phenomena.

2. Methods

[5] We used the Simple Biosphere model, Version 2 (SiB2) to estimate the terrestrial Net Ecosystem Exchange (NEE) for 1983 to 1993 on a global, 1° by 1° latitude/longitude grid with a 10-min time step [*Sellers et al.*, 1996a]. We investigated the effects of climate variability only and did not consider variability due to ocean uptake, fossil fuel emissions, land use, CO_2 fertilization, natural disturbances, or nitrogen deposition.

[6] SiB2 has high time resolution and detailed plant physiology to isolate the long-term influences of climate factors with strong diurnal variability, such as temperature and humidity. SiB2 uses the *Farquhar et al.* [1980] photosynthesis model scaled to the canopy level [*Sellers et al.*, 1996a], the Ball-Berry-Collatz stomatal conductance model [*Ball*, 1988; *Collatz et al.*, 1991, 1992], and the respiration model of *Denning et al.* [1996]. SiB2 accounts for the effects of snow cover, rainfall interception by the canopy, and aerodynamic turbulence [*Sellers et al.*, 1996a]. SiB2 separately tracks canopy and canopy air space prognostic variables (temperature, humidity, CO_2 concentration, etc.). As input, SiB2 requires Leaf Area Index (LAI), vegetation cover fraction, vegetation type, soil type, and weather data.

[7] We estimated LAI using global, 1° by 1° monthly composite maps of NDVI adjusted for missing data, satellite orbit drift, differing instrument calibrations, sensor degradation, and volcanic aerosols [*Sellers et al.*, 1994; *Los*, 1998; *Los et al.*, 2000]. Using remotely sensed LAI estimates simplified our model, since the observations already include the effects of age distribution, land use, and climate history. However, evaluating the effects of variability in biomass was more difficult since SiB2 does not track the various carbon and nitrogen pools. *Sellers et al.* [1994, 1996b] describes in detail the vegetation characteristics, soil types, and soil characteristics used as input. We used the *DeFries and Townshend* [1994] global map of 11 vegetation types.

[8] *Los et al.* [2000] assumed the vegetation cover fraction, f_V, was proportional to the absorbed fraction of photosynthetically active radiation (*fPAR*):

$$f_V = \frac{fPAR_{peak}}{fPAR_{\max}}, \tag{1}$$

where $fPAR_{peak}$ is the peak value of the absorbed fraction of PAR for each grid cell and $fPAR_{\max} = 0.95$ is the maximum possible *fPAR*. We estimated *fPAR* using an average between the simple ratio and NDVI methods [*Los et al.*, 2000]. *Los et al.* [2000] used the annual peak *fPAR*, which varies year-to-year, causing abrupt changes in f_V each January. An 11-year average $fPAR_{peak}$ artificially dampens variability in those years exceeding the average. We assumed f_V did not vary with time and used the $fPAR_{peak}$ for the entire 11-year period.

[9] Weather data were prescribed from the European Centre for Medium-Range Weather Forecasts (ECMWF) Reanalysis [*Gibson et al.*, 1999]. ECMWF Reanalysis contains surface temperature, pressure, wind speed, precipitation, and radiation data every 6 hours on a 1° by 1° grid. Except for the incident light, the ECMWF data was linearly interpolated between data points. The incident light was scaled by the cosine of the solar zenith angle to assure no light falls on the canopy at night while simultaneously conserving energy. ECMWF data were available for 1978 through 1993 and NDVI data for 1983 through 1999. Overlap between these two data sets limited this study to 1983 through 1993.

[10] NEE, the net flux of CO_2 from the terrestrial biosphere, is defined as

$$NEE = R - GPP, \tag{2}$$

where R is ecosystem respiration and GPP is gross primary production (i.e., canopy photosynthesis rate). Photosynthesis removes CO_2 from the atmosphere and respiration returns CO_2 to the atmosphere. A positive NEE indicates a net CO_2 flux into the atmosphere. GPP is resource-limited by Rubisco (nitrogen) capacity, available light, or leaf export capacity. Breaking R into autotrophic and heterotrophic respiration gives

$$NEE = R_H + R_R + R_C - GPP, \tag{3}$$

where R_H is heterotrophic respiration, R_R is root autotrophic respiration, and R_C is canopy autotrophic respiration. Heterotrophic respiration is the decay of organic material by microorganisms. Autotrophic respiration is the release of CO_2 during plant maintenance and growth. Defining ground respiration as $R_g = R_H + R_R$ and canopy net assimilation as A_n = GPP $- R_C$ gives:

$$NEE = R_g - A_n. \tag{4}$$

[11] R_g depends on soil temperature, soil moisture, and the mass of carbon in the respiring pools [*Parton et al.*, 1993; *Raich et al.*, 1991; *Hunt et al.*, 1996]. A serious technical issue arises when initializing the magnitudes of respiring carbon pools on a global, 1° by 1° grid. Two approaches used in the past are (1) "spinning up" from a state of zero carbon [e.g., *Potter et al.*, 1993] and (2) extrapolating from representative field studies [e.g., *Craig et al.*, 1998]. Spin up requires long integration times, because some of the soil carbon pools are very long-lived. *Randerson et al.* [1997] spun up the CASA model for 5000 simulated years before analyzing any results. Spin up has the advantage that ecosystem respiration and photosynthesis are everywhere balanced with respect to climate forcing, but is computationally prohibitive for our model (which uses a 10-min time step). Extrapolation is computationally efficient and allows for the possibilities of time-mean sources and sinks, but it is impossible to establish the veracity of global fields of biogeochemical pools defined everywhere from a few dozen field studies. *Craig et al.* [1998] used extrapolation and produced regional net sources and sinks of CO_2 in excess of 5 GtC/yr, which seems unreasonable.

[12] For our study, we adapted the respiration model of *Denning et al.* [1996], where the instantaneous value of R_g depends on soil temperature and moisture:

$$R_g = R^* R_f, \tag{5}$$

where R^* is a combined soil temperature and moisture scaling factor and R_f is the respiration factor. Following *Raich et al.* [1991], $R^* = f_T(T)\, f_W(W)$, where f_T is the temperature response function, T is temperature, f_W is the soil moisture response function, and W is the soil moisture fraction of saturation. R_g increases exponentially with soil temperature assuming $Q_{10} = 2.4$ [*Raich and Schlesinger*, 1992]. R_g increases with soil moisture to an optimum value then decreases (i.e., too much water and oxygen availability limits microbial growth) [*Raich et al*, 1991]. The optimal soil moisture, W_{opt}, varies between 0.6 and 0.7, depending on soil type. We calculate R^* separately for each of six soil layers and one layer of overlying litter.

[13] To allow for the dependence of respiration rates on carbon pool sizes, we assume photosynthesis and ecosystem respiration are everywhere in close balance on an annual timescale, but allow for perturbations due to interannual variability to persist over a specified relaxation time. This is parameterized by releasing accumulated carbon over a period of time, weighted by the temperature and soil moisture response functions. We chose a 1-year residence time so that the carbon cycle at every model grid cell is nearly in balance, but that perturbations in photosynthesis in one year are felt over the following year as perturbations in ecosystem respiration. R_f is the respiration rate that balances annual A_n when adjusted for soil temperature and water content:

$$R_f = \frac{\sum_{1\text{year}} A_n}{\sum_{1\text{year}} R^*}. \tag{6}$$

We divide the annual accumulated carbon among six soil layers and one litter layer based on the fraction of total roots in each layer. We assume the root density decreases exponentially with depth with biome specific profiles from *Jackson et al.* [1996]. We calculated a "rolling" R_f each month based on the previous 12 months of A_n and R^*.

[14] Four climate variables influence NEE in SiB2: temperature, precipitation, relative humidity, and incident light. We grouped them into those that effect GPP and those that effect R (Table 1). We listed precipitation and temperature twice because they affect both GPP and R. The SiB2 variables representing each climate variable change with the ECMWF weather data (which represents boundary layer values above the canopy), but also respond to changes in GPP and R and depend on the physical characteristics of the canopy and soil. For example, leaf surface humidity depends on plant transpiration, boundary layer humidity, and sensible heat flux. The influence of precipitation on GPP is limited to root zone soil moisture stress (i.e., drought stress).

[15] GPP and R also depend on the amount of biomass. LAI represents the above ground biomass and is prescribed via the input NDVI. The rolling R_f represents the effect of short-term variation in below ground biomass due to variations in GPP. We neglected the influence of LAI on autotrophic canopy respiration (R_C), since it rarely exceeds 5% of R and exerts only a 0.3% influence on NEE variability.

[16] To quantify how climate influences NEE variability, we calculated reference rates for GPP and R for each climate variable and compared them to the actual rate. We defined a climate variable influence as:

$$E_i = |\text{GPP}_i - \text{GPP}| \text{ or } E_i = |R_i - R|, \tag{7}$$

where E_i is the influence and GPP_i and R_i are reference rates for the ith climate variable. When a climate variable does not influence NEE, $E_i = 0$. For example, if GPP is Rubisco (nitrogen) limited and the light level increases, $E_{PAR} = 0$ since increased light would not affect GPP. The absolute value ensures nonnegative monthly averages of E_i. All E_i were calculated each time step and have units of flux.

Table 1. Climate Factors, SiB2 Variables, and Associated Reference Values

Climate Factor	Group	SiB2 Variable	Reference Value
Humidity	GPP	leaf surface relative humidity	1.0
Light	GPP	PAR incident on canopy top	200 W m^{-2}
Leaf Area Index	GPP	Leaf Area Index	LAI_{max}
Temperature	GPP	canopy temperature	298.15 K
Precipitation	GPP	root zone soil water fraction	1.0
Temperature	R	root zone soil temperature	298 K
Precipitation	R	root zone soil water fraction	W_{opt}
Soil carbon	R	respiration factor	R_{fmean}

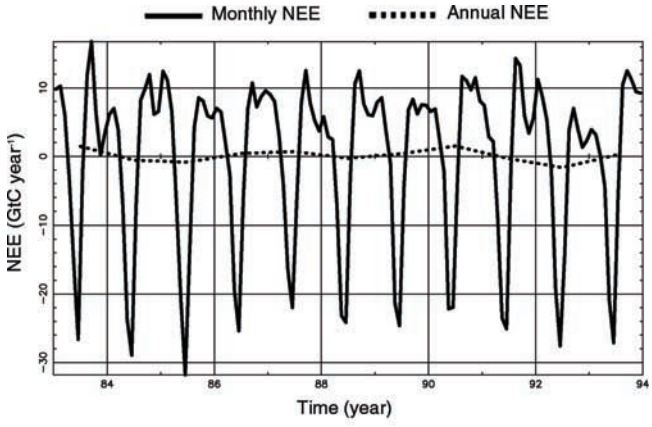

Figure 1. The Northern Hemisphere (NH) controls the seasonal changes in the simulated global NEE. Negative NEE spikes every June represent NH summer (GPP dominates NEE). The positive peak every September represents NH fall (respiration dominates NEE). The secondary minimum in November represents Southern Hemisphere (SH) spring. The annual NEE is near zero, but varies slightly year to year.

[17] To calculate the reference rate (GPP_i or R_i) for each E_i, we kept all inputs the same and changed the ith climate factor to a reference value as listed in Table 1. As humidity decreases, stomata close to minimize water loss, reducing GPP (i.e., humidity stress), so we chose the optimal humidity value of 1.0. For LAI, we chose the maximum possible LAI for each biome [*Sellers et al.*, 1996b]. For precipitation influence on GPP, we chose fully saturated soil ($W = 1.0$). For precipitation influence on R, we chose the optimal soil water content for maximum heterotrophic respiration, W_{opt} [*Raich et al.*, 1991]. For temperature influence on GPP and R, we chose reference values as identified in *Sellers et al.* [1996a]. For PAR we chose a typical saturated value (the canopy usually absorbs more light than it can use for photosynthesis). For soil carbon, we chose an average respiration factor, R_{fmean}, based on the mean seasonal variation of A_n and R^* (defined below).

[18] To assure E_i scales properly with GPP or R, (i.e., E_i is small when GPP is small and large when GPP is large), we calculated weighted monthly averages:

$$\overline{E_i} = \frac{\overline{\mathrm{GPP} \cdot E_i}}{\overline{\mathrm{GPP}}} \text{ or } \overline{E_i} = \frac{\overline{R \cdot E_i}}{\overline{R}}, \tag{8}$$

where the overbar represents a monthly average. The weighted monthly average influence, $\overline{E_i}$, measures the sensitivity of GPP and R (and thus NEE) to changes in the ith climate variable.

[19] We calculated the mean seasonal variation from global maps of monthly averages by averaging all Januaries, Februaries, etc. This resulted in 12 global maps (one for each month) representing the mean seasonal variation. Subtracting mean seasonal variation maps from monthly average maps produced monthly anomaly maps:

$$X' = \overline{X} = \widetilde{X}, \tag{9}$$

where X' is the monthly anomaly for variable X, $\overline{X}$ is the monthly mean of X, and $\widetilde{X}$ is the seasonal variation of X. From the anomaly maps, we produced maps of standard deviation, correlation, and other statistical parameters. Multiplying by grid cell area (which varies with latitude) and adding all land pixels produced total global land fluxes as a function of time.

3. NEE Variability

[20] The global land-surface NEE (GtC $year^{-1}$) shows a strong seasonal variation driven by vegetation in the Northern Hemisphere (Figure 1). The Northern Hemisphere has more land and vegetation than the Southern Hemisphere and dominates the global NEE seasonal cycle. NEE is most strongly negative during the Northern Hemisphere summer when global GPP is greatest. NEE is most strongly positive in Northern Hemisphere fall when assimilation drops off and global R dominates. The secondary minimum in November results from the surge in global GPP in the Southern Hemisphere spring. The NEE averages to zero over many years. However, small changes in GPP and R each year result in interannual NEE variability of about ±2 GtC $year^{-1}$.

[21] The simulated global NEE anomaly (GtC $year^{-1}$) as a function of time (Figure 2) captures most of the salient features of the measured global CO_2 growth rate extrapolated from flask measurements [*Conway et al.*, 1994]. The simulated NEE standard deviation (1.3 GtC $year^{-1}$) compares well with *Conway et al.* [1994] (1.1 GtC $year^{-1}$) and *Houghton* [2000] (1.0 GtC $year^{-1}$). The peaks and valleys roughly line up, but a 12-month running mean NEE shows only a weak correlation of 0.27 with the observed CO_2 growth rate. The simulated NEE lags behind the observed CO_2 growth rate by 2–3 months because we did not include transport from the terrestrial sources to the flask measurement sites. Accounting for transport lag only increases the correlation to 0.3 because the observed CO_2 growth rate accounts for variability in ocean fluxes, biomass burning, and fossil fuel emissions while we do not. Still, the

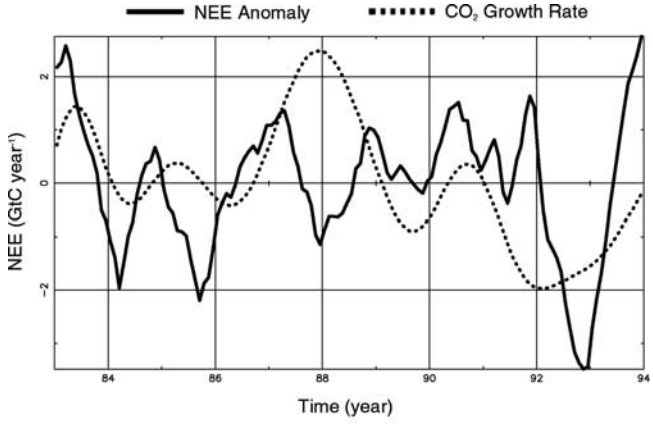

Figure 2. A 12-month running mean of the simulated global NEE anomalies captures the salient features and variability seen in anomalies of the measured global CO_2 growth rate.

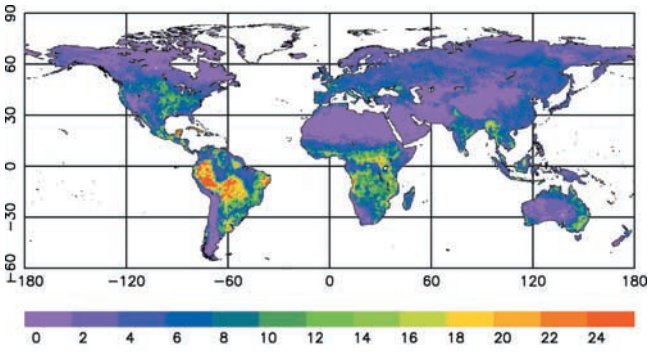

Figure 3. A map of NEE standard deviation (μg C m^{-2} s^{-1}) indicates grasslands of South America and Africa have the greatest interannual variability. The large anomaly in South America results from drought stress.

simulated NEE anomaly agrees fairly well with the global land flux estimates of *McGuire et al.* [2001] using several biogeochemical models, *Bousquet et al.* [2000] from inversion of flask measurements with a transport model, and *Kaduk and Heimann* [1997] from the long-term Mona Loa record.

[22] Some error in our simulated NEE may result from inaccuracies in NDVI estimates for tropical forests, which cover only 9% of the land surface, but account for 30% of global NEE. Spatial and temporal interpolation of NDVI data to account for persistent cloud cover over tropical forests artificially smooth LAI estimates, making it more difficult to predict year-to-year variations [*Los et al.*, 2000]. The CO_2 growth rate may not accurately account for land fluxes because the flask measurements sample predominantly marine rather than terrestrial air. Assuming a uniform 1-year turnover time introduces error into our NEE estimates since different biome types actually have different turnover times. Different turnover times for different biome types would change the timing of respiration anomalies, although the overall respiration variability would not change. Other sources of error include approximations in SiB2.

[23] A map of NEE standard deviation (Figure 3) shows that tropical grasslands in South America and Africa have the highest interannual variability followed by northern extratropical forests. Equatorial rain forests have fairly low variability except for the western half of the Amazon basin. The large South American anomaly results from precipitation variability from El Niño-Southern Oscillation (ENSO) and potential problems with the ECMWF precipitation data (see below). Although deserts are highly variable relative to their seasonal amplitude, low GPP results in low NEE standard deviations.

[24] Variability in the Northern extratropics is not as spatially uniform as implied in Figure 3. A typical map of simulated NEE anomalies for July 1984 (Figure 4) shows a pattern of alternating positive and negative regions across the Northern Hemisphere. The amplitudes of these simulated NEE anomalies range from 0.2 to 0.4 GtC yr^{-1} and are comparable to annual net carbon fluxes estimated from inversions of CO_2 flask measurements [e.g., *Bousquet et al.*, 2000; *Pacala et al.*, 2001]. The anomaly periods of 2–3 years are consistent with the 100% interannual variability seen by *Pacala et al.* [2001] in their estimates of the North American carbon sink. These regional anomalies tend to cancel, negating the effect of much greater land area in the Northern Hemisphere. While the Northern Hemisphere dominates the global NEE seasonal cycle, the tropics dominate global NEE interannual variability.

4. Climate Influences

[25] NEE anomalies depend on the relative magnitude of GPP and R anomalies because both respond in similar ways to climate and tend to cancel each other. For example, for a given soil water content, both GPP and R tend to increase with temperature. A climate anomaly will produce an NEE anomaly if either GPP or R responds more vigorously to climate variability. The relative magnitude of GPP and R variance measures how strongly they influence NEE interannual variability:

$$f_{\mathrm{GPP}} = \sigma_{\mathrm{GPP}}^2/\left(\sigma_{\mathrm{GPP}}^2 + \sigma_R^2\right) \quad \text{or} \quad f_R = \sigma_R^2/\left(\sigma_{\mathrm{GPP}}^2 + \sigma_R^2\right), \tag{10}$$

where f_{GPP} and f_R are the relative influences of GPP and R on NEE interannual variability, σ_{GPP} and σ_R are the standard deviations of GPP and σ_{GPP}^2 and R, and σ_{GPP}^2 and σ_R^2 are the variances of GPP and R. When $f_R = 0$, respiration has no influence on NEE interannual variability; when $f_R = 1$, respiration totally controls NEE variability (by definition, $f_{\mathrm{GPP}} = 1 - f_R$).

[26] R dominates NEE variability at high latitudes (Figure 5) while GPP and R exert roughly equal influences in the highly variable tropical grasslands. Although GPP variability almost totally controls the deserts, these regions have such low GPP they do not significantly affect the global NEE interannual variability. Overall, R accounts for 59% and GPP for 41% of the global NEE interannual variability.

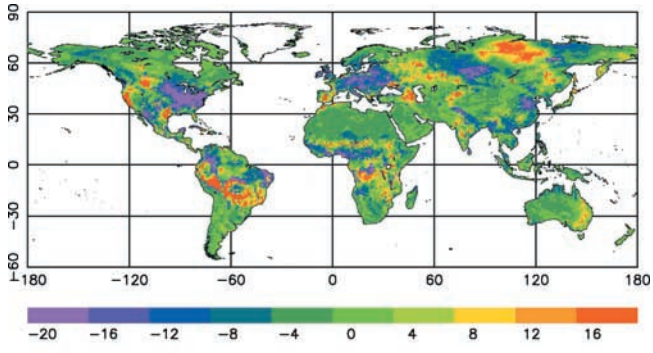

Figure 4. A map of typical simulated NEE anomalies (μg C m^{-2} s^{-1}) for July 1984 shows a pattern of alternating positive and negative regions across the Northern Hemisphere. These regional anomalies tend to cancel such that the tropics dominate global NEE interannual variability.

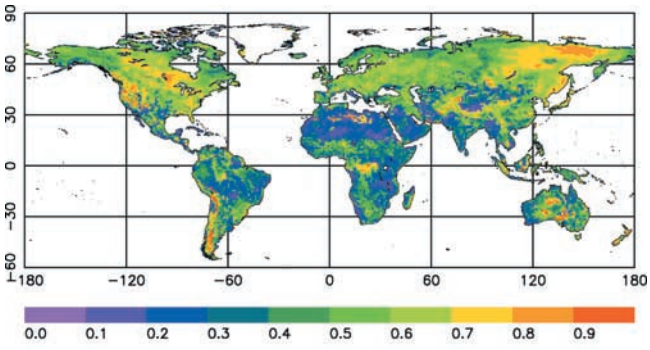

Figure 5. A map of the relative influence of respiration on NEE interannual variability (0 means no influence, 1 means total control) indicates respiration dominates in high latitudes. GPP and respiration exert roughly equal influence in the tropics. The relative influences of respiration and GPP are based on the relative magnitudes of their variances.

[27] Isolating the causes for these regional differences is difficult because the climate variables are coupled and do not vary independently of one another. Feedback between climate variables often limits NEE variability. For example, increasing canopy temperature increases GPP, but also decreases relative humidity (which decreases GPP). Comparing relative magnitudes of $\overline{E}_i$ variance accounts for such cancellation and feedback between climate factors. The total influence of the GPP E_i group on NEE variability cannot exceed the relative influence of GPP itself such that

$$f_i = \frac{\sigma_i^2}{\sum \sigma_i^2} f_{\mathrm{GPP}} \quad \text{or} \quad f_i = \frac{\sigma_i^2}{\sum \sigma_i^2} f_R, \tag{11}$$

where f_i is the interannual influence of the ith climate factor and σ_i^2 the variance of $\overline{E}_i$. When $f_i = 0$, the climate factor has no influence and when $f_i = 1$, the climate factor totally controls NEE interannual variability. By definition, the sum of all f_i for both the R and GPP groups equals one $\left(\sum f_i = 1\right)$. Maps of f_i show strong regional differences in the influence of climate on NEE variability (Figure 6).

[28] Precipitation control of GPP (Figure 6a) and R (Figure 6b) dominate throughout the tropics. The GPP and R precipitation influence patterns do not significantly overlap. The demarcation lies roughly where the average soil moisture equals W_{opt}. This division is especially clear in regions with a strong spatial gradient in soil moisture (e.g., sub-Saharan Africa and South America). The soil moisture influence on GPP represents drought stress. In semi-arid and desert regions with drier soils ($W < W_{opt}$), precipitation control of GPP dominates because respiration can occur even in very dry soils while GPP ceases below minimum soil water content. In nearly saturated soils ($W > W_{opt}$), precipitation changes effect respiration, but do not induce drought stress, so precipitation control of R dominates. *Tian et al.* [1998] saw a similar dependency in their simulation of NEE in the Amazon basin.

[29] The large NEE anomaly in South America (Figure 3) may result from problems with the ECMWF precipitation data as well as naturally occurring drought stress. Spatial patterns of precipitation differ between datasets derived from rain gauge data and those from reanalysis using a model [*Costa and Foley*, 1998]. Our simulated anomaly differs slightly from that simulated by *Tian et al.* [1998] because they used precipitation based on rain gauge data. The precipitation data from the ECMWF reanalysis is diagnostic and unconstrained by rain gauge measurements. The spectral representation of topography in ECMWF produces false undulations in the land surface, creating potentially suspect precipitation anomalies in South America [*Costa and Foley*, 1998]. Bright NDVI data may indicate plant growth, but the ECMWF may systematically put the rain somewhere else, resulting in drought stress.

[30] Temperature influence on respiration dominates NEE variability at high latitudes (Figure 6d). The temperature response function for R is exponential, so small soil temperature anomalies can produce large R anomalies, especially during peak temperatures in the summer. By contrast, GPP is relatively insensitive to temperature except at extreme high and low temperatures (Figure 6c). The resulting temperature influence on GPP is very small and reflects variability in temperature extremes at high latitudes, high altitudes, and deserts. Essentially, R goes up and down with temperature relative to a more stable GPP.

[31] LAI influences NEE interannual variability in tropical grasslands, high-latitude forests and tundra (Figure 6e). The LAI influence represents the indirect effect of climate (precipitation, temperature, snow cover, etc.) on plant growth, probably when the ecosystem is most sensitive, such as spring [*Houghton*, 2000]. In general, snow cover influences LAI in the high northern latitudes, temperature in the midlatitudes, and a combination of precipitation and temperature in the tropics [*Los et al.*, 2001].

[32] Soil carbon has a fairly evenly distributed influence on NEE interannual variability, peaking at the equator and decreasing toward the poles (Figure 6f). Like LAI, soil carbon represents the indirect effects of climate on soil organic matter due to GPP anomalies. The resulting soil carbon anomalies last a year because of the assumed 1-year turnover time in the rolling respiration factor. Consequently, regions where GPP dominates NEE variability also show a strong soil carbon influence.

[33] Humidity shows a weak, but fairly uniform influence on NEE interannual variability (Figure 6g). Transpiration during photosynthesis generally keeps the leaf surface humidity near saturation, making it insensitive to changes in ECMWF humidity (defined in the boundary layer above the canopy). Humidity influences GPP only when high sensible heat flux mixes relatively dry boundary layer air down into the canopy, reducing the humidity at the leaf surface and causing humidity stress.

[34] Although globally weak, PAR shows a fairly strong regional influence in equatorial tropical forests where persistent cloud cover reduces the light available for plant growth (Figure 6h). In SiB2, photosynthesis is light-limited

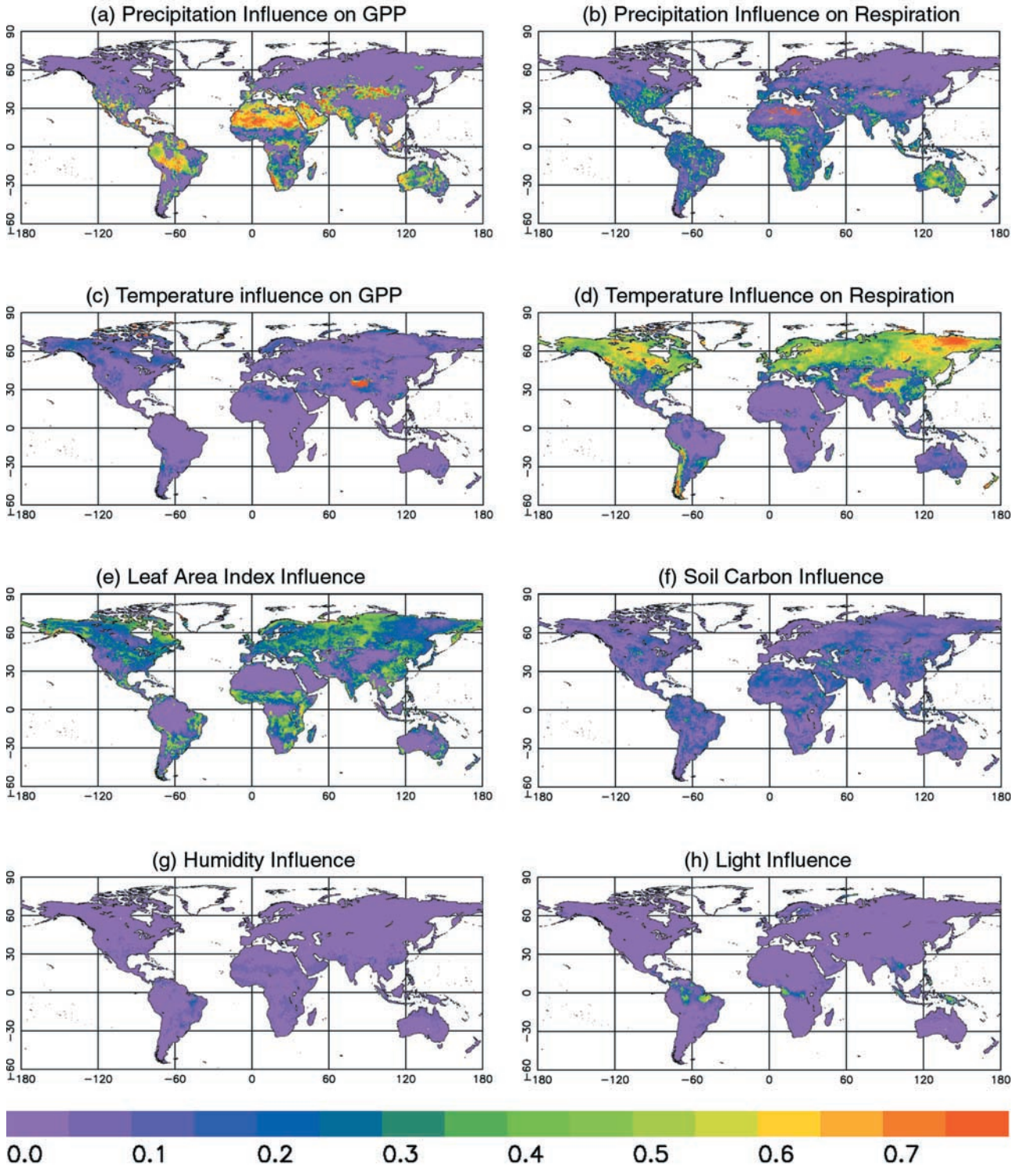

Figure 6. The relative influences of each climate factor on the simulated NEE interannual variability show strong regional differences. The influences are based on relative magnitudes of variance for each climate factor (0 means no influence, 1 means total control). Precipitation influence on GPP via soil moisture dominates in tropical grasslands and deserts. Temperature influence on respiration dominates at high latitudes. LAI influence represents climate influences during plant growth. The incident light influences NEE variability only in regions of extensive rainfall. Soil carbon has the greatest influence in the tropics. Humidity exerts a fairly uniform, but weak global influence.

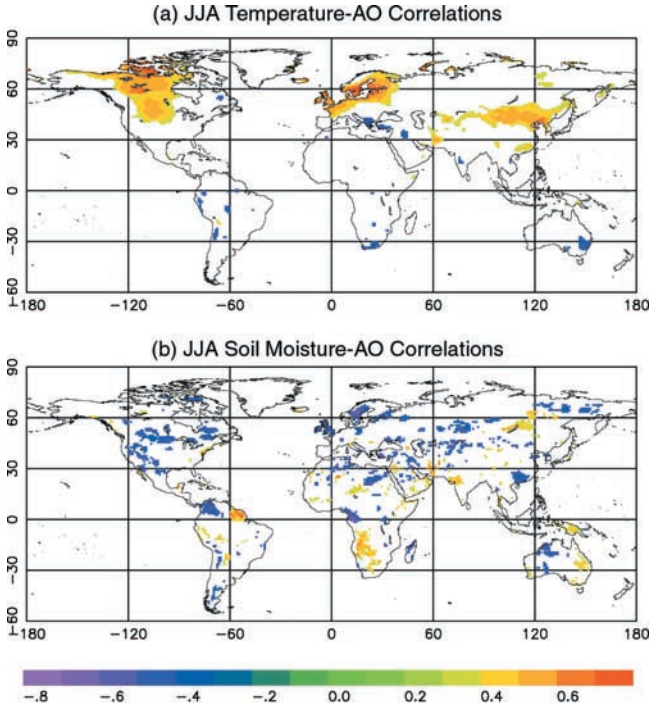

Figure 7. The Arctic Oscillation (AO) advects warm oceanic air into continental interiors, resulting in positive temperature and negative soil moisture correlations in northern Europe, central Canada and central Asia. We focused on June–July–August (JJA) because 50% of all Northern Hemisphere NEE anomalies occur in the summer. Southern Hemisphere correlations probably do not reflect direct AO influence.

only at low light levels in the early morning and late evening (PAR below about 100 W m^{-2}). At other times, nitrogen or export capacity limit GPP. The length of time each day that GPP is light-limited determines the overall influence of PAR. Precipitation anomalies change the cloud cover and incident PAR, which determines the time each day when GPP is light-limited.

[35] Because of the regional cancellation in the Northern Hemisphere, precipitation in the tropics dominates the simulated global NEE interannual variability seen in Figure 2. Precipitation influence on GPP and *R* combined account for 44% of the global NEE variability (precipitation influence on GPP accounts for 32% while precipitation influence on *R* accounts for 12%). Variability in LAI and soil carbon combined account for 35% of global NEE variability (23% and 12%, respectively). Overall humidity and PAR influences on global NEE variability are very weak (2% and 3%, respectively). Temperature accounts for 16% of the global NEE interannual variability. The temperature influence on GPP is weak (1% globally). Despite dominating the Northern Hemisphere, regional cancellation reduces the global influence of temperature on respiration to 15% of the simulated global NEE variability. Having quantified these influences, we examined in detail two climatic phenomena known to effect interannual variability in temperature and precipitation: the Arctic Oscillation and the El Niño-Southern Oscillation.

5. Arctic Oscillation and NEE Variability

[36] The Arctic Oscillation (AO) is characterized by a north-south dipole in the strength of the zonal wind between 35°N and 55°N [*Thompson and Wallace*, 2000, 2001]. Positive AO polarity has stronger westerly winds north of 45°N and weaker winds south of 45°N, which favors increased advection of relatively warm oceanic air deep into continental interiors. Negative AO polarity has weaker mean zonal flow and more blocking, pulling cold Arctic air masses down into continental interiors. Positive AO polarity produces positive temperature anomalies over land; negative polarity produces negative anomalies. Since the AO primarily influences the Northern Hemisphere and since 50% of all Northern Hemisphere NEE anomalies occur in summer, we focused our analysis on June–July–August (JJA).

[37] Figure 7 shows summer (JJA) correlations of air temperature and soil moisture with an AO index based on the first principle mode of sea level pressure anomalies from the NCEP reanalysis [*Thompson and Wallace*, 2000]. Figure 8 shows JJA correlations of GPP, *R*, and NEE with the AO index. The AO index, GPP, and temperature data show positive trends for 1983–1993 [*Los*, 1998; *Thompson et al.*, 2000], which we removed prior to correlation. We omitted correlations failing the t-test at 95% significance [*Devore*, 1995]. The degrees of freedom for the t-test are based on the total number of summer months in our simulation (assuming each month is independent). Warm air advection associated with positive AO polarity shows up as positive temperature correlations in northern Europe, Canada, and central Asia. The reduced blocking associated with positive AO polarity deceases rainfall in the same regions, resulting in negative soil moisture correlations.

[38] Figure 8 indicates the AO signal is strongest in northern Europe for GPP and *R*, but competing effects and cancellation result in weak AO correlations with NEE. As seen in Figure 6, several climate factors control NEE variability in Northern Europe: temperature (via GPP and *R*), LAI, precipitation (via *R*), and humidity. Decreased *R* due to reduced soil moisture partially cancels increased *R* due to higher temperatures. Decreased GPP due to increased humidity stress partially cancels increased GPP due to warmer temperatures. The result is modest positive AO correlations with *R* and GPP. While both GPP and *R* increase with temperature, *R* responds more vigorously. The GPP anomalies partially cancel the *R* anomalies, resulting in weak positive NEE correlations. Similar cancellation occurs in Canada and central Asia resulting in even weaker NEE correlations with the AO. Correlations scattered throughout the Southern Hemisphere are probably random associations and do not reflect direct influence by the AO.

[39] Overall, temperature effects from the AO dominate over precipitation effects. The limited spatial extent of the AO influence combined with cancellation effects result in a very weak AO signal in the NEE variability in summer. The

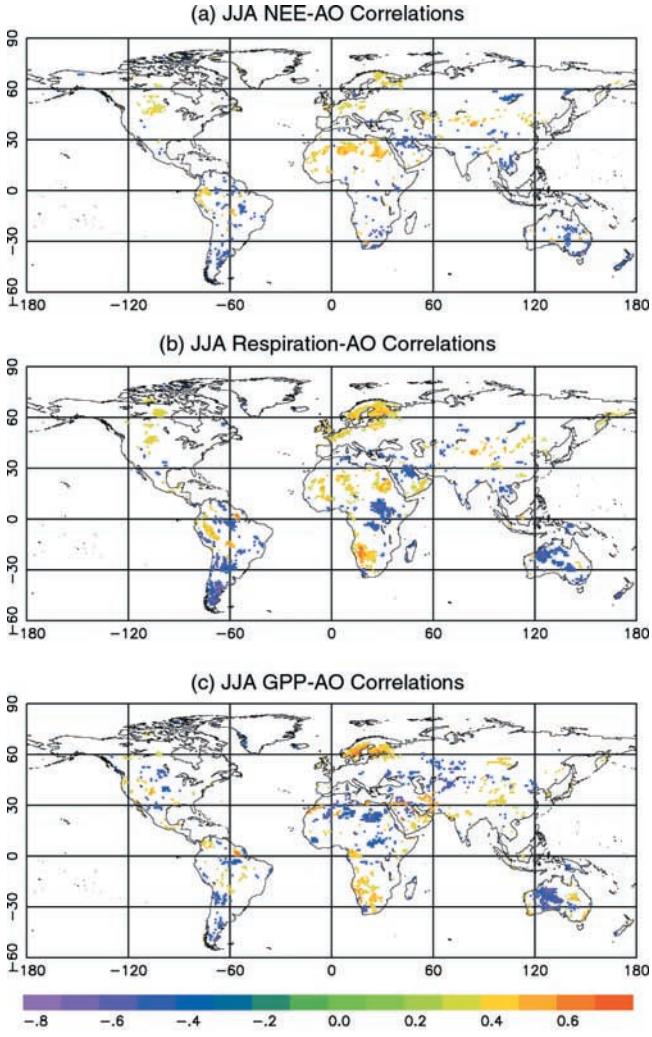

Figure 8. Respiration and GPP anomalies often cancel, resulting in very weak correlations between the Arctic Oscillation (AO) and NEE. The strongest AO signal is in Northern Europe. Southern Hemisphere correlations probably do not reflect direct AO influence.

AO can explain part of the strong temperature influence across the Northern Hemisphere and the Northern Europe portion of the simulated spatial pattern for NEE, but not the 2–3 year cycle in NEE variability.

6. ENSO and NEE Variability

[40] El Niño-Southern Oscillation (ENSO) is characterized by weaker or stronger trade winds in the equatorial Pacific. Weaker trade winds (El Niño) cut off cold-water upwelling off of South America and shift the Pacific warm water pool from off Asia eastward to the central Pacific. Strong trade winds (La Niña) push the Pacific warm pool westward toward Australia. El Niño and La Niña are the extremes of alternating sea level pressures between east and west Pacific known as the Southern Oscillation. The Pacific warm pool moving with ENSO has a domino effect, shifting rainfall and temperature patterns around the globe [*Green et al.*, 1997]. ENSO has a period of 2–7 years. Our simulation covered two El Niño events and part of a third (1982–1983, 1986–1987, and 1991–1992) and two La Niña events (1984–1985, 1988–1989).

[41] Figure 9 shows correlations of air temperature and soil moisture with a Southern Oscillation Index (SOI) based on the sea level pressure difference between Tahiti and Darwin for 1983–1993. We removed trends and omitted correlations failing the t-test at 95% significance. Negative SOI corresponds to El Niño; positive SOI corresponds to La Niña. Negative correlations mean increases during El Niño; positive correlations mean decreases during El Niño.

[42] Rainfall patterns throughout the tropics shift as the Pacific warm pool moves east and west with ENSO. For example, rainfall (and thus soil moisture) in Australia drops during El Niño as the Pacific warm pool moves to the east, resulting in positive SOI correlations. Decreased rainfall reduces cloud cover, increases solar heating, and reduces evaporative cooling [*Kaduk and Heimann*, 1997], which increases temperature and produces negative SOI correlations. Temperature is fairly constant in the tropics, so although the correlations appear strong, the effect is small. In East Russia, reduced cloud cover associated with reduced precipitation during El Niño increases radiative cooling, decreasing temperatures and producing positive SOI correlations. In summary, ENSO primarily affects global precipitation and soil moisture patterns and weakly influences temperature.

[43] The effects of shifting rainfall patterns on GPP and *R* can cancel (Figure 10). For example, in Australia and India, both *R* and GPP show positive correlations with SOI (both

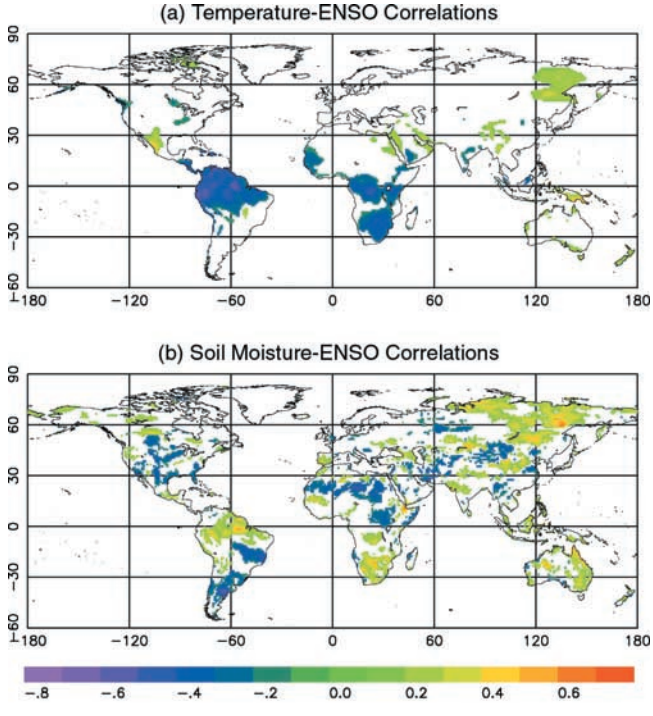

Figure 9. Correlations with a Southern Oscillation Index indicate ENSO strongly influences global precipitation patterns, especially in the tropics.

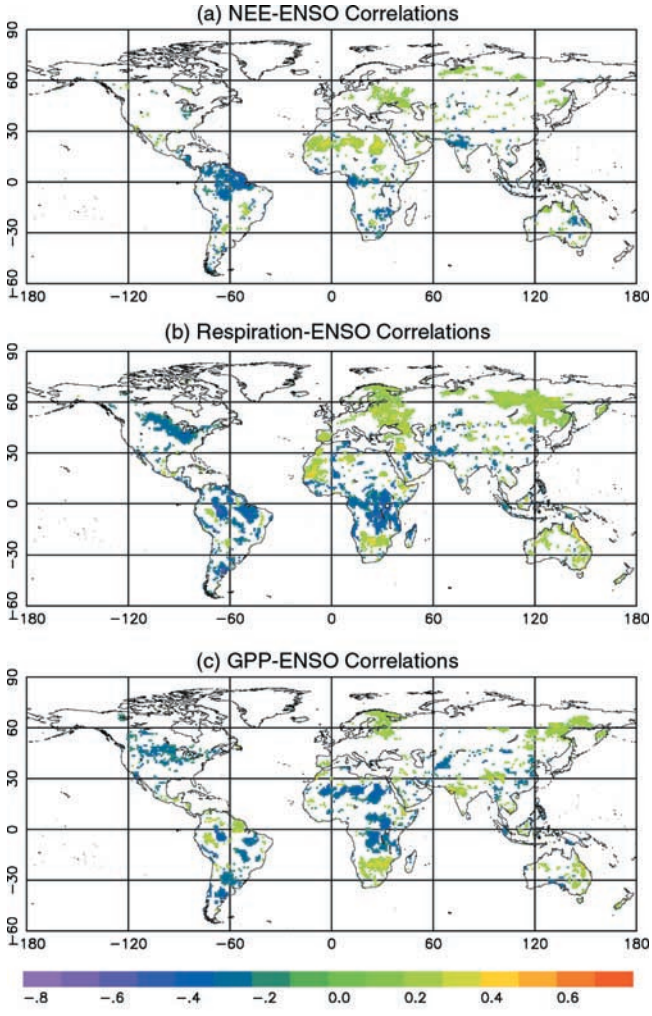

Figure 10. Correlations with a Southern Oscillation Index indicate ENSO influences NEE variability primarily in the tropics, consistent with expected shifts in precipitation.

decrease as precipitation drops during El Niño). Precipitation controls NEE variability for Australia and India (Figures 6a and 6b). Areas controlled by drought stress show negative NEE correlations (R > GPP during El Niño). Areas controlled by soil moisture for respiration show positive NEE correlations (R < GPP during El Niño). Zero NEE correlations indicate the R and GPP anomalies cancel.

[44] The large NEE anomaly in South America (Figure 4) results from drought stress due to rainfall shifting with ENSO. The soil water content relative to the optimum for respiration, W_{opt}, drives the spatial pattern of this anomaly. The average soil water content exceeds W_{opt} in the Amazon basin and decreases southward and westward to less than W_{opt} in the highlands of central and western South America. During El Niño, rainfall shifts from the Amazon basin and central South America to the west and southeast. The soil water in the Amazon basin decreases and respiration increases, but GPP is not affected, resulting negative correlations for R and NEE, but weak correlations for GPP. In the central South American highlands, the soil water is less than W_{opt}, so decreased rain during El Niño reduces R and introduces drought stress, resulting in positive R and GPP correlations. Drought stress coupled with possible problems with the ECMWF precipitation data (described above) produce a highly variable NEE anomaly, but partial cancellation between GPP and R weakens the NEE correlation with ENSO.

[45] The ENSO influence above 30°N is weak. Temperature variability due to ENSO shows up as a strong correlation with R in east Russia. The high values of LAI influence on NEE variability (Figure 6g) and corresponding high soil moisture correlations indicate ENSO influences snow cover, melting times, and spring plant growth [*Kaduk and Heimann*, 1997; *Los et al.*, 2001] in Europe and Canada. This may partly explain the simulated NEE anomaly pattern in the Northern Hemisphere. However, ENSO does not explain the strong temperature influence across the Northern Hemisphere or the 2–3 year cycle in NEE variability.

[46] Overall, ENSO primarily affects NEE variability in the tropics through changes in precipitation, explaining much of the NEE variability simulated in South America, Africa, and Asia. While our correlations are statistically significant at 95% assuming each month is independent, our simulation covers only three ENSO cycles. Our results are consistent with that expected from ENSO, but a more rigorous analysis requires simulations of several decades.

7. Conclusions

[47] The global NEE from our simulation captured the salient features of the observed global CO_2 growth rate. The detailed process information and high time resolution in SiB2 allowed us to isolate and quantify the influences of climate on global and regional interannual variability of NEE. Further, using remotely sensed LAI we estimated the overall influence of plant biomass on GPP variability. Assuming a 1-year turnover time we estimated the effect of below ground biomass on respiration variability. Using biome specific turnover times would improve the timing of respiration anomalies. Adding an ocean model would improve the match with the observed CO_2 growth rate. Explicitly tracking various carbon and nitrogen pools would isolate the effects of land use, growing season length, nitrogen availability, and other factors that influence NEE interannual variability.

[48] The tropical grasslands in South America and Africa show the highest NEE variability. The large South American NEE anomaly is driven by shifting precipitation with ENSO, but may also result, in part, from ECMWF precipitation errors. The simulated NEE in the Northern Hemisphere shows a pattern of alternating positive and negative anomalies with periods of 2–3 years and amplitudes consistent with inversions of CO_2 flask measurements. The alternating anomalies tend to cancel such that the tropics control global NEE interannual variability while the Northern Hemisphere controls the global NEE seasonal cycle.

[49] Because of cancellation and competing effects, no single climate variable controls global or regional NEE interannual variability. Precipitation exerts the greatest

influence (44% of global NEE variability), followed by LAI (23%), temperature (16%), and soil carbon (12%). Humidity and available light do not strongly influence global NEE variability. Climate influences have strong regional differences: temperature influence on respiration dominates in the extratropics while precipitation influence on GPP and R dominates in the tropics. For regions controlled by precipitation the soil water content relative to W_{opt} determines whether GPP or R controls NEE variability. In dry soils ($W < W_{opt}$), GPP dominates; in wet soils ($W > W_{opt}$), R dominates.

[50] The influence of ENSO on NEE variability is consistent with that expected for shifting precipitation patterns in the tropics, especially for the large South American anomaly. A definitive assessment requires a longer time record, since our simulation covered only three ENSO cycles. Except in northern Europe, temperature advection by the AO does not significantly influence NEE variability. Neither the AO nor ENSO fully explain the temperature influence on respiration or the simulated NEE anomaly pattern in the Northern Hemisphere.

[51] **Acknowledgments.** This research was funded through the University of California at Berkeley under NASA grant SA2805-23941 and through the University of California at Santa Barbara under NASA Cooperative Agreement NCC5-302, the Earth System Science Workbench (ESSW): a scalable infrastructure for Earth Science Information Partners (ESIPs). We thank Thomas Conway of the National Oceanic and Atmospheric Administration, Climate Monitoring and Diagnostics Laboratory, Boulder, Colorado for supplying the CO_2 growth rate data. We thank David Thompson of the Atmospherics Sciences Department, Colorado State University for valuable advice and insight regarding our analysis of the Arctic Oscillation.

References

Ball, J. T., An analysis of stomatal conductance, Ph.D. thesis, Stanford University, Stanford, Calif., 1988.

Bousquet, P., P. Peylin, P. Ciais, C. Le Quéré, P. Friedlingstein, and P. Tans, Regional changes in carbon dioxide fluxes of land and oceans since 1980, *Science*, *290*, 1342–1346, 2000.

Collatz, G. J., J. T. Ball, C. Grivet, and J. A. Berry, Physiological and environmental regulation of stomatal conductance, photosynthesis, and transpiration: A model that includes a laminar boundary layer, *Agric. For. Meteorol.*, *54*, 107–136, 1991.

Collatz, G. J., M. Ribascarbo, and J. A. Berry, Coupled photosynthesis-stomatal conductance model for leaves of C4 plants, *Aust. J. Plant Physiol.*, *19*(5), 519–538, 1992.

Conway, T. J., P. P. Tans, L. S. Waterman, K. W. Thoning, D. R. Kitzis, K. A. Masarie, and N. Zhang, Evidence for interannual variability of the carbon cycle from the National Oceanic and Atmospheric Administration/Climate Monitoring and Diagnostics Laboratory Global Air Sampling Network, *J. Geophys. Res.*, *99*(D11), 22,831–22,855, 1994.

Costa, M. H., and J. A. Foley, A Comparison of Precipitation Data sets for the Amazon Basin, *Geophys. Res. Lett.*, *25*(2), 155–158, 1998.

Craig, S. G., K. J. Holmén, G. B. Bonan, and P. J. Rasch, Atmospheric CO_2 simulated by the National Center for Atmospheric Research Community Climate Model, 1, Mean fields and seasonal cycles, *J. Geophys. Res.*, *103*(D11), 13,213–13,235, 1998.

Defries, R. S., and J. R. G. Townshend, NDVI-derived land cover classification at a global scale, *Int. J. Remote Sens.*, *15*(17), 3567–3586, 1994.

Denning, A. S., G. J. Collatz, C. Zhang, D. A. Randall, J. A. Berry, P. J. Sellers, G. D. Colello, and D. A. Dazlich, Simulations of terrestrial carbon metabolism and atmospheric CO_2 in a general circulation model, 1, Surface carbon fluxes, *Tellus, Ser. B*, *48*, 521–542, 1996.

Devore, J. L., *Probability and Statistics for Engineering and the Sciences*, Duxbury, Boston, Mass., 1995.

Dickinson, R. E., How coupling of the atmosphere to ocean and land helps determine the timescales of interannual variability of climate, *J. Geophys. Res.*, *105*(D15), 20,115–20,119, 2000.

Farquhar, G. D., S. von Caemmerer, and J. A. Berry, A biochemical model of photosynthetic CO2 assimilation in leaves of C3 species, *Planta*, *149*, 78–90, 1980.

Fung, I., Variable carbon sinks, *Science*, *290*, 1313, 2000.

Gibson, J. K., S. Uppala, P. Kållberg, M. Fiorino, A. Hernandez, K. Onogi, and X. Li. ECMWF 40-year Re-Analysis (ERA-40)–Archive Plans, report, Eur. Cent. For Medium-Range Weather Forecasts, Reading, England, 1999.

Goetz, S. J., S. D. Prince, J. Small, and A. C. R. Gleason, Interannual variability of global terrestrial primary production: Results of a model driven with satellite observations, *J. Geophys. Res.*, *105*(D15), 20,077–20,091, 2000.

Green, P. M., D. M. Legler, C. J. Miranda V, and J. J. O'Brien, The North American climate patterns associated with El Niño-Southern Oscillation, *Project Rep. Ser. 97-1*, Cent. for Ocean-Atmos. Predict. Stud., Fla. State Univ., Tallahassee, Fla., 1997.

Houghton, R. A., Interannual variability in the global carbon cycle, *J. Geophys. Res.*, *105*(D15), 20,121–20,130, 2000.

Houghton, R. A., E. A. Davidson, and G. M. Woodwell, Missing sinks, feedbacks, and understanding the role of terrestrial ecosystems in the global carbon balance, *Global Biogeochem. Cycles*, *12*(1), 25–34, 1998.

Hunt, E. R., Jr., S. C. Piper, R. Nemani, C. D. Keeling, R. D. Otto, and S. W. Running, Global net carbon exchange and intraannual atmospheric CO_2 concentrations predicted by an ecosystem process model and three-dimensional atmospheric transport model, *Global Biogeochem. Cycles*, *10*(3), 431–456, 1996.

Ichii, K., Y. Matsui, Y. Yamaguchi, and K. Ogawa, Comparison of global net primary production trends obtained from satellite-based normalized difference vegetation index and carbon cycle model, *Global Biogeochem. Cycles*, *15*(2), 351–363, 2001.

Jackson, R. B., J. Canadell, J. R. Ehleringer, H. A. Mooney, O. E. Sala, and E. D. Schulze, A global analysis of root distributions for terrestrial biomes, *Oecologia*, *108*, 389–411, 1996.

Kaduk, J., and M. Heimann, Assessing the climate sensitivity of the global terrestrial carbon cycle model SILVAN, *Phys. Chem. Earth*, *21*(5–6), 529–535, 1997.

Le Quéré, C., J. C. Orr, P. Monfray, O. Aumont, and G. Madec, Interannual variability of the ocean sink of CO_2 from 1979 through 1997, *Global Biogeochem. Cycles*, *14*(4), 1247–1265, 2000.

Lloyd, J., Current perspectives on the terrestrial carbon cycle, *Tellus, Ser. B*, *51*, 336–342, 1999.

Los, S. O., Linkages between global vegetation and climate: An analysis based on NOAA advanced very high resolution radiometer data, *1998-206852*, NASA Goddard Space Flight Cent., Greenbelt, Md., 1998.

Los, S. O., G. J. Collatz, P. J. Sellers, C. M. Malmström, N. H. Pollack, R. S. DeFries, C. J. Tucker, L. Bounoua, M. T. Parris, and D. A. Dazlich, A global 9-year biophysical land surface data set from NOAA AVHRR data, *J. Hydrometeorol.*, *1*(2), 183–199, 2000.

Los, S. O., G. J. Collatz, L. Bounoua, P. J. Sellers, and C. J. Tucker, Global interannual variations in sea surface temperature and land-surface vegetation, air temperature, and precipitation, *J. Clim.*, *14*, 1535–1549, 2001.

McGuire, A. D., et al., Carbon balance of the terrestrial biosphere in the twentieth century: Analyses of CO_2 climate and land use effects with four process-based ecosystem models, *Global Biogeochem. Cycles*, *15*(1), 183–206, 2001.

Pacala, W., et al., Consistent land-and ocean-based U. S. carbon sink estimates, *Science*, *292*, 2316–2320, 2001.

Parton, W. J., et al., Observations and modeling of biomass and soil organic matter dynamics for the grassland biome worldwide, *Global Biogeochem. Cycles*, *7*(4), 785–809, 1993.

Potter, C. S., and S. A. Klooster, Detecting a terrestrial biosphere sink for carbon dioxide: Interannual ecosystem modeling for the mid-1980s, *Clim. Change*, *42*(3), 489–503, 1999.

Potter, C. S., J. T. Randerson, C. B. Field, P. A. Matson, P. M. Vitousek, H. A. Mooney, and S. A. Klooster, Terrestrial ecosystem production: A process-oriented model based on global satellite and surface data, *Global Biogeochem. Cycles*, *7*(4), 811–842, 1993.

Prince, S. D., S. N. Goward, S. Goetz, and K. Czajkowski, Interannual atmosphere-biosphere variation: Implications for observation and modeling, *J. Geophys. Res.*, *105*(D15), 20,055–20,063, 2000.

Raich, J. W., and W. H. Schlesinger, The global carbon dioxide flux in soil respiration and its relationship to vegetation and climate, *Tellus, Ser. B*, *44*, 81–99, 1992.

Raich, J. W., E. B. Rastetter, J. M. Melillo, D. W. Kicklighter, P. A. Steudler, and B. J. Peterson, Potential net primary production in South America: Application of a global model, *Ecol. Appl.*, *1*(4), 399–429, 1991.

Randerson, J. T., M. V. Thompson, T. J. Conway, I. Y. Fung, and C. B. Field, The contribution of terrestrial sources and sinks to trends in the

seasonal cycle of atmospheric carbon dioxide, *Global Biogeochem. Cycles*, *11*(4), 535–560, 1997.

Rayner, P. J., and R. M. Law, The interannual variability of the global carbon cycle, *Tellus, Ser. B*, *51*, 210–212, 1999.

Sarmiento, J. L., Atmospheric CO_2 stalled, *Nature*, *356*, 697–698, 1993.

Sellers, P. J., C. J. Tucker, G. J. Collatz, S. O. Los, C. O. Justice, D. A. Dazlich, and D. A. Randall, A global 1° by 1° NDVI data set for climate studies, 2, The generation of global fields of terrestrial biophysical parameters from NDVI, *Int. J. Remote Sens.*, *15*(17), 3519–3545, 1994.

Sellers, P. J., D. A. Randall, G. J. Collatz, J. A. Berry, C. B. Field, D. A. Dazlich, C. Zhang, G. D. Collelo, and L. Bounoua, A revised land surface parameterization of GCMs, I, Model formulation, *J. Clim.*, *9*, 676–705, 1996a.

Sellers, P. J., S. O. Los, C. J. Tucker, C. O. Justice, D. A. Dazlich, G. J. Collatz, and D. A. Randall, A revised land surface parameterization of GCMs, II, The generation of global fields of terrestrial biophysical parameters from satellite data, *J. Clim.*, *9*, 706–737, 1996b.

Tans, P. P., and D. W. R. Wallace, Carbon cycle research after Kyoto, *Tellus, Ser. B*, *51*, 562–571, 1999.

Thompson, D. W. J., and J. M. Wallace, Annular modes in the extratropical circulation, I, Month-to-month variability, *J. Clim.*, *13*, 1000–1016, 2000.

Thompson, D. W. J., and J. M. Wallace, Regional climate impacts of the Northern Hemisphere annular mode, *Science*, *293*, 85–89, 2001.

Thompson, D. W. J., J. M. Wallace, and G. Hegerl, Annular modes in the extratropical circulation, II, Trends, *J. Clim.*, *13*, 1018–1036, 2000.

Tian, H., J. M. Melillo, D. W. Kicklighter, A. D. McGuire, J. V. K. Helfrich III, B. Moore III, and C. J. Vorosmarty, Effect of interannual climate variability on carbon storage in Amazonian ecosystems, *Nature*, *396*, 664–667, 1998.

Trolier, M., W. C. White, P. P. Tans, K. A. Masarie, and P. A. Gemery, Monitoring the isotopic composition of atmospheric CO_2: Measurements from the NOAA Global Air Sampling Network, *J. Geophys. Res.*, *101*(D20), 25,897–25,916, 1996.

I. Baker, A. S. Denning, L. Prihodko, K. Schaefer, and N. Suits, Colorado State University, Department of Atmospheric Sciences, Fort Collins, CO 80523-1371, USA. (baker@atmos.colostate.edu; denning@atmos.colostate.edu; lara@atmos.colostate.edu; Kevin@atmos.colostate.edu; nsuits@atmos.colostate.edu)

J. Kaduk, Department of Geography, University of Leicester, Leicester, LE1 7RH, England, UK. (J.Kaduk@Leicester.ac.uk)

S. O. Los, Department of Geography, University of Wales, Swansea, Singleton Park, Swansea, SA2 8PP, Wales, UK. (s.o.los@swan.ac.uk)